ELSEVIER

J. Non-Newtonian Fluid Mech. 122 (2004) 131–146

Journal of Non-Newtonian Fluid Mechanics

www.elsevier.com/locate/jnnfm

Numerical simulation of compressible viscoelastic liquids

I.J. Keshtiban, F. Belblidia, M.F. Webster*

Department of Computer Science, Institute of Non-Newtonian Fluid Mechanics, Singleton Park, University of Wales, Swansea SA2 8PP, UK

Received 9 July 2003; received in revised form 5 November 2003; accepted 15 December 2003

This article is part of a Special Volume containing papers from the XIIIth International Workshop on Numerical Methods in Viscoelastic Flows

Abstract

A time-marching pressure-correction/Taylor–Galerkin finite element algorithm is presented to accommodate low Mach number compressible and incompressible viscoelastic liquid flows. The algorithm is based on an operator splitting constructive process that discloses three fractional stages. For the compressible regime, a piecewise-constant density interpolation with gradient recovery is employed, for which the background theory and consistency of approach are discussed. The scheme is applied to contraction flows for Oldroyd model fluids, covering entry–exit flows and high pressure-drop situations. Stability and performance characteristics of the new algorithmic implementation are highlighted. Solutions are provided for a range of compressible settings, tending to the incompressible limit at vanishing Mach number.

Keywords: Compressible liquid; Viscoelastic; Finite element; Taylor–Galerkin; Pressure-correction; Low Mach number; Oldroyd-B

1. Introduction

In our previous studies [1], we have presented a scheme capable of simulating weakly-compressible and incompressible *viscous* flows. There, the scheme was applied successfully to several benchmark test problems. In the compressible scenario, one observes spatial convergence-rates that reach a third-order for continuous problems. The algorithm performs well at low to vanishing Mach number (*Ma*), leading to the emergence of a unified scheme for both compressible and incompressible viscous flows. The aim of the present study is seen as a natural extension into the viscoelastic regime, to accommodate compressible and incompressible liquid flows, based upon the Oldroyd-B model fluid. We consider stability, accuracy and performance of the compressible viscoelastic algorithm for low to zero Mach number situations (approaching the incompressible limit). In addition, we conduct a parameter sensitivity analysis to assess convergence history for Weissenberg number (*We*) levels of order unity and for flows starting from quiescent initial conditions. We begin by providing some motivation for the present study.

Low Mach number flows play an important role, occurring widely in nature and in many industrial processes. In polymer processing operations, such as injection modelling and high-speed extrusion, pressure and flow rate may be large. Hence, compressibility effects within the viscoelastic regime may become important and influence resulting flow phenomena. From a physical perspective, the difference between incompressible and compressible flows lies in the propagation of longitudinal acoustic waves transmitted through the flow. For incompressible flows, the speed of such longitudinal waves approaches infinity, whereas the speed of transverse waves is finite. In contrast, for compressible flows, the speed of both waves takes on finite values. Moreover, this is manifest through a switch in equation type depending on the particular flow setting (incompressible to compressible). For example, within the unsteady viscous regime, the equations for compressible flow form a hyperbolic–parabolic system, whilst those for incompressible flow assume an elliptic–parabolic system. Nevertheless, it is preferable to work within a unified framework to accommodate algorithmically, in an automated fashion, with such type change. In the present study, this idea

* Corresponding author. Tel.: +44 1792 295656; fax: +44 1792 295708.
E-mail address: m.f.webster@swansea.ac.uk (M.F. Webster).

0377-0257/$ – see front matter © 2004 Elsevier B.V. All rights reserved.
doi:10.1016/j.jnnfm.2003.12.008

is pursued, based on local Mach number considerations, yet being capable of handling low Mach numbers, extending to the incompressible limit ($Ma \approx 0$).

Comprehensive literature reviews for viscoelastic incompressible flow may be found in Baaijens [2], Crochet et al. [3], Keunings [4] and Walters and Webster [5]. A variety of formulations have been developed over the last decade or so, such as finite volume (FV) methods [6,7], finite element method [8–11], spectral collocation methods [12] and hybrid finite element/finite volume (FE/FV) methods [13,14]. This would include time-marching and steady-state approaches, leading to various options for the state-of-the-art (e.g. DEVSS [11], Discontinuous-Galerkin and Galerkin-Least-Squares [2], and others). The context of compressible viscous flow at low Mach number was covered extensively in our precursor study [1]. There, two principal numerical approaches were highlighted, being of density-based and pressure-based construction. Apropos this context, numerical computation meets a significant challenge: transcending from low Mach numbers towards the zero Mach number, singular limiting state. The compressible viscoelastic domain is relatively unchartered in the literature. Georgiou [15] has addressed non-Newtonian inelastic (Carreau) fluid modeling for compressible flows, with particular interest in slip effects at the wall, relevant to time-dependent Poiseuille flow and extrudate-swell. Brujan [16] has derived an equation of motion for bubble dynamics, incorporating the effects of compressibility and viscoelastic proprieties for an Oldroyd-B model fluid. The objective there has been to analyse the physics of cavitation. Mackley and co-workers [17] has reported on experimental data in the multi-pass rheometer (MPR), taking into account compressibility in time-dependent capillary flow measurements for a high-density polyethylene melt (HDPE), linking this to pressure adjustment in the system. In Barrett and Gotts [18], the equations of motion have been transformed into the Laplace domain to analyse a compressible dynamic viscoelastic hollow sphere problem.

From a numerical standpoint, the present formulation extends an incompressible fractional-staged time-stepping procedure to accommodate compressible viscoelastic flow regimes, for low to vanishing Mach number. This presents advance upon our earlier studies for viscoelastic incompressible flows [9], incorporating some recent developments adopted from the compressible viscous context [1]. The present formulation incorporates a semi-implicit Taylor–Galerkin/pressure-correction (TGPC) technique for mass and momentum, with a combination of two-step Lax-Wendroff and Crack-Nicolson time discretization procedures. This is a second-order pressure-correction scheme, solving for the temporal increment of pressure on the time-step. The discretization of stress is accomplished via a streamline-upwinding Taylor–Petrov–Galerkin technique, with velocity gradient recovery and hence, compatibility between stress and velocity gradient solution spaces. The equation of state for density represents the pressure dependence within the system, through the well-established modified form of the Tait model [19]. In the finite element representation, based upon our earlier observations and without loss of accuracy [1], density is interpolated in a piecewise-constant form (incompressible per element), with nodal recovery applied for density gradients.

At present, in the development of the algorithm, we restrict attention to isothermal flows. On a benchmark example of 4:1 planar contraction flow, we illustrate how the algorithm can meet the challenge of representing both compressible and incompressible liquid flows. We follow how algorithmic extension into the compressible regime has influenced the characteristics of the original incompressible implementation, particularly via convergence proprieties to steady-state and order of accuracy (in space and time [1]). The flow problem considered is that for an Oldroyd-B model, where it is acknowledged that a limiting Weissenberg number (Wecrit) will be met.

The present article is organized as follows: the governing equations for compressible viscoelastic flow for Oldroyd-B model fluid are expounded in Section 2. In Section 3, we introduce the fractional equation stages of the Taylor–Galerkin/pressure-correction scheme, followed by the finite element (FE) spatial discretization adopted. In Section 4, we document solutions generated for the benchmark contraction flow test-problem. The schemes proposed are validated for consistency and accuracy via mesh refinement. Comparison against incompressible counterparts and the literature complements the high-order of accuracy achieved. This ranks above second-order for smooth flows. Careful attention is paid to temporal convergence histories for flows starting from quiescent initial conditions, attaining solutions at a unit level of Weissenberg number. Various strategies are highlighted to improve numerical convergence properties, specifically when dealing with the incompressible flow scenario.

2. Compressible viscoelastic flow–governing equations

The governing equations for compressible viscoelastic flow under isothermal conditions may be represented through conservation of mass and momentum, in conjunction with constitutive equation for stress and equation of state for density. The balance equations of mass and momentum[1] may be expressed in non-dimensional form, using standard differential operator notation and independent variables of time, t, and space, x:

$$\frac{\partial \rho}{\partial t} + \nabla(\rho U) = 0, \tag{1}$$

$$Re\,\rho \frac{\partial U}{\partial t} = \left[\nabla\left(2\frac{\mu_s}{\mu}d + \tau\right) - Re\,\rho U.\nabla U - \nabla P\right], \tag{2}$$

[1] Non-conservative form, see Hirsh [20].

where U, τ, P represent dependent variables of velocity, extra-stress and pressure, and ∇U the velocity gradient. Material properties are described through liquid density, ρ, relaxation time, λ (see below), and viscosity, μ. The total viscosity may be split into Newtonian (solvent), μ_s and polymeric (elastic), μ_e contributions, such that $\mu = \mu_s + \mu_e$. Non-dimensional parameters adopted are $\mu_s^* = \mu_s/\mu = 1/9$ and, $\mu_e^* = \mu_e/\mu = 8/9$ and there is need to define the tensor $d_{ij} = [(\nabla U + (\nabla U)^T)/2] - 1/3\,[(\nabla U)]\delta_{ij}$, as would emerge naturally from the physics.

We adopt the Oldroyd-B model fluid to characterise stress response, through the constitutive equation:[2]

$$We\,\frac{\partial \tau}{\partial t} = -We\,(U\cdot\nabla\tau - \tau\cdot\nabla U - (\tau\cdot\nabla U)^T) + 2\mu_e^* d - \tau. \tag{3}$$

The dimensionless group numbers are those of Reynolds number and Weissenberg number, defined according to convention as,

$$Re = \frac{\rho_0 U_0 l_0}{\mu}, \quad We = \frac{\lambda U_0}{l_0}. \tag{4}$$

Such dimensionless form is obtained by introducing characteristic scales on density ρ_0, viscosity μ, length l_0 (exit half-channel width), velocity U_0 (exit flow, average velocity), λ and the single relaxation time of the Oldroyd model-fluid. Note, for incompressible flow with constant density, the continuity equation reduces to $\nabla U = 0$:

To represent compressibility, we appeal to the modified Tait equation of state [19], to relate density to pressure, viz.,

$$\frac{\tilde{P} + B}{\tilde{P}_0 + B} = \left(\frac{\rho}{\rho_0}\right)^m,$$

where augmented pressure,

$$\tilde{P} = P - \frac{1}{3}\,\mathrm{trace}\,(\tau + 2\mu_s^* d). \tag{5}$$

Here, power-index m and constant B are scalar parameters, and denote reference scale for pressure. Note, in a strict sense, Eq. (5) is exact only for isentropic change. Although in the present analysis, the energy equation has been discarded,[3] the Tait equation may be applied to reasonable precision more generally, since m and B are independent of entropy, is constant [16]. This state law is often approximated to a linear form with index m set to unity [21], an over-simplification which we may expose. After rearranging and differentiating the equation of state, we gather:

$$\frac{\partial \tilde{P}}{\partial \rho} = m\rho^{m-1}\frac{(\tilde{P}_0 + B)}{\rho_0^m} = \frac{m(\tilde{P} + B)}{\rho} = c_{(x,t)}^2, \tag{6}$$

where $c_{(x,t)}$ represents the speed of sound. By employing the chain rule upon Eq. (6) and taking difference operations over the time-step $\Delta t = (t_{n+1} - t_n)$, we may relate density increment to pressure increment at time instant t_{n+1} through,

$$\frac{\Delta\rho^{n+1}}{\Delta t} = \frac{1}{c_{(x,t)}^2}\frac{\Delta\tilde{P}^{n+1}}{\Delta t}. \tag{7}$$

We have recourse to such a relationship below in the derivation of the particular fractional-stage equations, to realise a compressible temporal evolutionary expression for pressure (see reference [1] for more details). Henceforth, for clarity we discard yet imply (*) notation on viscosity fractions and (∼) notation on pressure. At this point we may define Mach number as $Ma = U/c$, being the ratio of fluid velocity to the speed of sound.

3. Taylor–Galerkin/pressure-correction scheme and FE discretization

The general framework of the Taylor–Galerkin/pressure-correction scheme is based on a time-stepping procedure, involving two distinct phases within each time step. The *first phase* involves a Taylor–Galerkin scheme, expounded through a two-step, Lax-Wendroff time stepping procedure. This represents a predictor–corrector doublet for velocity and stress, which initially calculates predicted fields $(U, \tau)^{n+1/2}$, prior to computing a non-divergence-free velocity field U^* and an updated stress field τ^{n+1}. The *second phase* is a pressure-correction scheme that ensures second-order accuracy in time. This generates an equation for temporal pressure-difference and a Poisson equation in incompressible flow. A *third* and *final phase* is a correction stage that recaptures the velocity field at the end-of-time step loop. By implementing a semi-implicit Crack–Nicolson treatment for diffusion terms, a semi-discrete incremental form of the TGPC scheme may be derived, devoid of heavy stability restriction imposed through diffusion operators. This scheme may be presented in a three-fractional stage form viz.,

Stage-1a.

$$2Re\rho\frac{U^{n+\frac{1}{2}} - U^n}{\Delta t} = [\nabla(2\mu_s D + \tau) - Re\rho U.\nabla U]^n - \nabla P^n + \nabla\cdot\mu_s(D^{n+\frac{1}{2}} - D^n), \tag{8}$$

$$2We\frac{\tau^{n+\frac{1}{2}} - \tau^n}{\Delta t} = [2\mu_e D - \tau - We\{U\cdot\nabla\tau - \tau\cdot\nabla U - (\tau\cdot\nabla U)^T\}]^n, \tag{9}$$

Stage-1b.

$$Re\rho\frac{U^* - U^n}{\Delta t} = [\nabla\cdot\tau - Re\rho U\cdot\nabla U]^{n+\frac{1}{2}} + [\nabla(2\mu_s D) - \nabla P]^n + \nabla\mu_s(D^* - D^n), \tag{10}$$

[2] Note, the recommended use of the full-generalised form of d in the UCM constitutive model by Oliveira et al. [8] for expediency in numerical convergence, even within the incompressible state.

[3] Here, we are interested in low Reynolds number isothermal flows, where kinetic energy considerations are negligible.

$$We\frac{\tau^{n+1}-\tau^{n+\frac{1}{2}}}{\Delta t} = [2\mu_e D - \tau - We\{U\cdot\nabla\tau - \tau\cdot\nabla U - (\tau\cdot\nabla U)^T\}]^{n+\frac{1}{2}}, \quad (11)$$

Stage-2.

$$\frac{1}{c^2_{(x,t)}}\frac{P^{n+1}-P^n}{\Delta t} - \Delta t\theta\nabla^2(P^{n+1}-P^n) = -[\rho^n\nabla.U^* + \nabla\rho^n.U^*], \quad (12)$$

Stage-3.

$$Re\rho\frac{U^{n+1}-U^*}{\Delta t} = -\theta\nabla(P^{n+1}-P^n). \quad (13)$$

Note the momentum equations for compressible and incompressible flows are practically identical, bar variation in density. Differences emerge due to the various alternative forms of the continuity equation. Hence, Eq. (12) displays some notable features (see [1] for detailed derivation): the first term on the left-hand-side is a first-order time derivative representation, whilst the second term is governed by a Laplacian operator (elliptic properties). In addition, on the right-hand-side, density is a direct function of pressure, that is to be interpreted via the Tait equation of state. When the flow is incompressible, the speed of sound asymptotes to infinity. In this context, the first term on the left-hand-side vanishes along with the second term on the right-hand-side, and elliptic character dominates Eq. (12). Alternatively, switching to compressible flows, the balance of equation-type-domination adjusts between elliptic and hyperbolic, the extent of type-mix depending upon the Mach number level (local compressibility).

A Galerkin finite element spatial discretization is adopted, based on triangular elements in two dimensions. This employs a piecewise continuous quadratic interpolation $\phi(x)$ for velocity and stress, and linear interpolation $\psi(x)$ for pressure, of the form:

$$U(x,t) = U_j(t)\phi_j(x),\ \tau(x,t) = T_j(t)\phi_j(x), \quad j = 1,6$$
$$\text{and } P(x,t) = P_k(t)\psi_k(x), \quad k = 1,3. \quad (14)$$

Time-dependent velocity, stress and pressure nodal-vectors are represented as $U(t)$, $T(t)$ and $P(t)$, respectively. For density, piecewise-constant interpolation over an element is considered, which necessitates recovery to gather density gradient representation [9]. Recovery is imposed per vertex node for density, conducting averaging over all elements surrounding each node. From such nodal values, density gradients may be gathered per vertex node from the underlying linear interpolation functions, a relatively swift cost-effective procedure. Comparison between piecewise-constant and linear density implementations is considered elsewhere [1], where the piecewise-constant form emerges as the more pragmatic choice.

As alluded to above, stability of the scheme is enhanced by appealing to a semi-implicit version of the scheme. The discretized equation for compressible viscoelastic flow may be expressed in fully-discrete matrix form, via TGPC-stages 1–3, viz.

Stage-1a.

$$\left[2Re\frac{M_\rho}{\Delta t} + \frac{\mu_s}{2}S_U\right](U^{n+\frac{1}{2}} - U^n) = \{-[\mu_s S_U + ReN_\rho(U)]U - BT\}^n + L^T P^n, \quad (15)$$

$$2We\frac{M}{\Delta t}(T^{n+\frac{1}{2}} - T^n) = [2\mu_e M(L+L^T) - \{M + WeN(U)\}T + We\{N_e(T)L + (N_e(T)L)^T\}]^n, \quad (16)$$

Stage-1b.

$$\left[Re\frac{M_\rho}{\Delta t} + \frac{\mu_s}{2}S_U\right](U^* - U^n) = \{-[\mu_s S_U + ReN_\rho(U)]U - BT\}^{n+\frac{1}{2}} + L^T P^n, \quad (17)$$

$$We\frac{M}{\Delta t}(T^{n+1} - T^n) = [2\mu_e M(L+L^T) - \{M + WeN(U)T + We\}\{N_e(T)L + (N_e(T)L)^T\}]^{n+\frac{1}{2}}, \quad (18)$$

Stage-2.

$$\left[\frac{M_C}{\Delta t} + \theta\Delta t K\right](P^{n+1} - P^n) = -L^\rho U^* \quad (19)$$

Stage-3.

$$Re\frac{M_\rho}{\Delta t}(U^{n+1} - U^*) = \theta L^T(P^{n+1} - P^n) \quad (20)$$

where

$$(M_\rho)_{ij} = \int_\Omega \rho\phi_i\phi_j\,d\Omega, \qquad (M)_{ij} = \int_\Omega \phi_i\phi_j\,d\Omega,$$
$$(M_C)_{ij} = \int_\Omega \frac{\psi_i\psi_j}{c^2_{(x,t)}}\,d\Omega \quad (21)$$

$$(N_\rho)_{ij} = \int_\Omega \rho\phi_i(U\nabla\phi_j)d\Omega, \qquad (N)_{ij} = \int_\Omega \phi_i(U\nabla\phi_j)d\Omega,$$
$$(N_e)_{ij} = \int_\Omega \phi_i(T\nabla\phi_j)d\Omega, \quad (22)$$

$$(B)_{ij} = \int_{\Omega} \phi_i \nabla\phi_j \, \mathrm{d}\Omega, \qquad (K)_{ij} = \int_{\Omega} \nabla\psi_i \nabla\psi_j \, \mathrm{d}\Omega, \tag{23}$$

$$(L_k)_{ij} = \int_{\Omega} \psi_i (\nabla\phi_j)_k \, \mathrm{d}\Omega,$$
$$(L_k^{\rho})_{ij} = \int_{\Omega} \psi_i \left\{ \psi_l \rho_l \frac{\partial\phi_j}{\partial x_k} + \frac{\partial\psi_l}{\partial x_k} \rho_l \phi_j \right\} \mathrm{d}\Omega, \tag{24}$$

$$(S_U)_{ij} = (S_{lm})_{ij}, \quad l, m = 1, 2$$
$$(S_{11})_{ij} = \int_{\Omega} \left(2\frac{\partial\phi_i}{\partial x}\frac{\partial\phi_j}{\partial x} + \frac{\partial\phi_i}{\partial y}\frac{\partial\phi_j}{\partial y} - \frac{2}{3}\frac{\partial\phi_i}{\partial x}\frac{\partial\phi_j}{\partial x} \right) \mathrm{d}\Omega, \tag{25}$$

$$(S_{12})_{ij} = \int_{\Omega} \frac{\partial\phi_i}{\partial y}\frac{\partial\phi_j}{\partial x} \, \mathrm{d}\Omega,$$
$$(S_{22})_{ij} = \int_{\Omega} \left(\frac{\partial\phi_i}{\partial x}\frac{\partial\phi_j}{\partial x} + 2\frac{\partial\phi_i}{\partial y}\frac{\partial\phi_j}{\partial y} - \frac{2}{3}\frac{\partial\phi_i}{\partial y}\frac{\partial\phi_j}{\partial y} \right) \mathrm{d}\Omega, \tag{26}$$

Algebraic solvers for such systems are dealt with extensively elsewhere [22,23]. Briefly, a direct solution method is employed at the pressure equation stage-2, whilst a space-efficient element-by-element Jacobi iteration is invoked over the remaining stages one and three. The element-by-element iteration avoids full system matrix construction and the mass-matrix iteration that results (m_{itn}) is normally performed only 3–5 times.

From a computational standpoint, the main modification introduced to the incompressible TGPC scheme (see reference [9]) to handle the compressible regime has arisen at stage-2. This is achieved by the introduction of the two new matrices M_C and L^{ρ}, governed by compressibility considerations. Introduction of M_C implies variation of the stage-2 pressure matrix per time-step, demanding a fresh decomposition and back-substitution per time-step as with free-surface/domain-shifting problems. This leads to 30% more computational time per time-step than in the incompressible instance, but may be avoided through delayed explicit reference on the previous time-step. The form of L^{ρ} in expression (24) indicates the need for density gradient evaluation (term, $\partial\psi_l/\partial x_k$ see above).

In addition, in the definition of the diffusion matrix S_U, an additional term is appended $[(-2/3)(\partial\phi_i/\partial x)(\partial\phi_j/\partial x)]$ within S_{11}, and likewise, $[(-2/3)(\partial\phi_i/\partial y)(\partial\phi_j/\partial y)]$ in S_{22}. With piecewise-constant density interpolation over an element, some matrix simplification [4] arises: $(M_{\rho})_{ij} = \sum_{\Omega_{\mathrm{e}}} \rho_{\mathrm{e}} (M^{\mathrm{e}})_{ij}$ and $(N_{\rho})_{ij} = \sum_{\Omega_{\mathrm{e}}} \rho_{\mathrm{e}} (N^{\mathrm{e}})_{ij}$, where $(M^{\mathrm{e}})_{ij} = \int_{\Omega_{\mathrm{e}}} \phi_i \phi_j \, \mathrm{d}\Omega_{\mathrm{e}}$ and $(N^{\mathrm{e}})_{ij} = \int_{\Omega_{\mathrm{e}}} \phi_i (U \cdot \nabla\phi_j) \, \mathrm{d}\Omega_{\mathrm{e}}$. We note that the incompressible second stage of the TGPC scheme collapses to:

$$[\theta \Delta t K](P^{n+1} - P^n) = -LU^*. \tag{27}$$

This completes our discourse on scheme derivation and discretization issues.

4. Scheme implementation and numerical solutions

The benchmark problem of flow through an abrupt 4:1 contraction for an Oldroyd-B fluid is recognised as a formidable test problem, in terms of stability at high Weissenberg number. It is well-documented in the literature on viscoelastic incompressible flow (for example, see references: [5,24]). Here, it is chosen to validate our asymptotic 'zero' Mach number solutions against published incompressible results. In addition, consistency, accuracy and behaviour of the more compressible solutions are monitored for high levels of Weissenberg number. For this problem, the total length of the planar channel is 76.5 units (see Fig. 1). No-slip boundary conditions are assumed on solid boundaries. At the inlet, transient boundary conditions (bc) are imposed reflecting build-up through flow-rate (Waters and King, (W&K) [25]), generating set transient profiles for normal velocity (U_x) and stress (τ_{xx}, τ_{xy}), displaying vanishing cross-sectional components in velocity (U_y) and stress (τ_{yy}). The mathematical specification for these profiles is given in Carew et al. [26], with dependence upon Weissenberg number. This provides smooth growth of driving boundary conditions, at any particular *We*, and improves numerical stability in convergence to steady-state. True transients may be accessed from suitable start-up fields in this manner. Step increments would apply correspondingly, if incremental continuation through *We*-solutions is employed. In contrast, at the exit, weak-form natural boundary conditions are established, via boundary integrals (B.I.) and momentum equation representation, where once more, U_y vanishes. A pressure reference level is set to zero at the outlet. We take advantage of flow symmetry about the horizontal central axis running through the domain, computing solutions on half the problem domain. Reynolds number is set to unity allowing some inertia to enter the problem. To accommodate different flow regimes, our strategy has been to alter the values of the Tait parameter-set (m,B). These have been adjusted between those representing low compressible flow conditions, say (4,10^2) representative of maximum $Ma = O(10^{-1})$, to a highly incompressible state, typically (10^4,10^4) representative of maximum $Ma = O(10^{-4})$. Then, corresponding solutions may be compared unequivocally to those for incompressible prevailing assumptions.

[4] $(M_{\rho})_{ij} \int_{\Omega} \rho\phi_i\phi_j \, \mathrm{d}\Omega_{\mathrm{e}} = \sum_{\Omega_{\mathrm{e}}} \left(\int_{\Omega_{\mathrm{e}}} \rho\phi_i\phi_j \, \mathrm{d}\Omega_{\mathrm{e}} \right) = \sum_{\Omega_{\mathrm{e}}} \left(\rho_{\mathrm{e}} \int_{\Omega_{\mathrm{e}}} \phi_i\phi_j \, \mathrm{d}\Omega_{\mathrm{e}} \right) = \sum_{\Omega_{\mathrm{e}}} \rho_{\mathrm{e}} (M^{\mathrm{e}}_{ij})$.

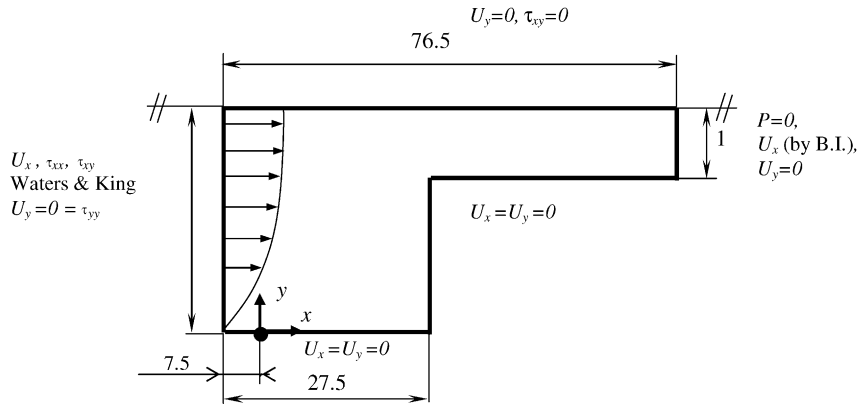

Fig. 1. Contraction flow schema.

Table 1
Mesh characteristic parameters

	M1	M2	M3
Elements	980	1140	2987
Nodes	2105	2427	6220
Vertex nodes	563	644	1617
d.o.f.	8983	9708	14057
Corner mesh density	28	63	201
R_{min}	0.024	0.023	0.006
R_{max}	0.126	0.131	0.095

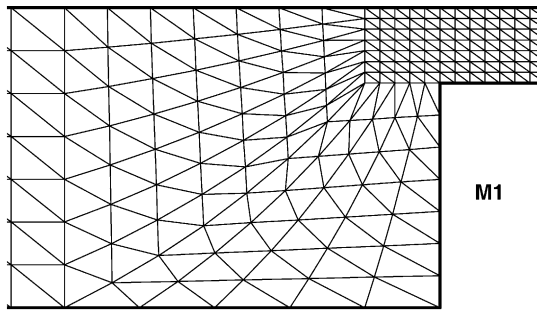

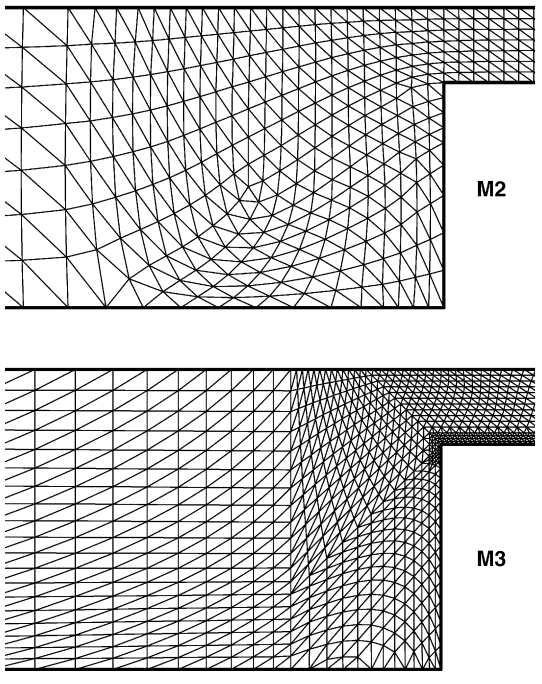

Fig. 2. Mesh refinement around the contraction, M1–M3 (mesh characteristics in Table 1).

4.1. Trends in temporal convergence history

The unified framework may be assessed with respect to time-stepping convergence history tolerance to steady-state and spatial accuracy properties. To this end, three different meshes are employed, M1, M2 and M3, covering increasing levels of refinement (h) within the contraction zone. Triangular element mesh structure is illustrated in Fig. 2 and mesh characteristics are quantified in Table 1, where details are recorded for total numbers of elements, nodes, degrees of freedom, corner mesh density and minimum and maximum element size (see also, Baloch et al. [8] and Matallah et al. [9]). Here, a multi-block meshing strategy is employed, with conformal mapping in each sub-block and matching of boundary nodes at interfaces. To access the time-stepping convergence history a temporal relative-increment L_2-norm is defined to govern time-stepping convergence history against a set tolerance, Tol_t, viz.,

$$E^T(X) = \frac{||X^{n+1} - X^n||}{1 + ||X^{n+1}||} \leq \mathrm{Tol}_t. \tag{28}$$

4.1.1. Numerical parameter sensitivity analysis (compressible flow)

First, within the compressible context, we conduct a numerical parameter sensitivity analysis on time-step (Δt) and mass iteration number (m_{itn}), setting the Tait parameter pairing to (m,B) = (4,10^2). Here, computational testing is based on mesh M1, with Weissenberg number set to unity and commencing from initial conditions (ic) of a quiescent state. History tolerance results governing pressure ($\mathrm{E}^{\mathrm{T}}(P)$), velocity ($\mathrm{E}^{\mathrm{T}}(U)$) and stress ($\mathrm{E}^{\mathrm{T}}(T)$) are displayed in Fig. 3. The relevant parameter values are those of: (t = 10^{-2}, 10^{-3}, 10^{-4}; and m_{itn} = 1, 3 and 5. For the compressible flow setting, re-

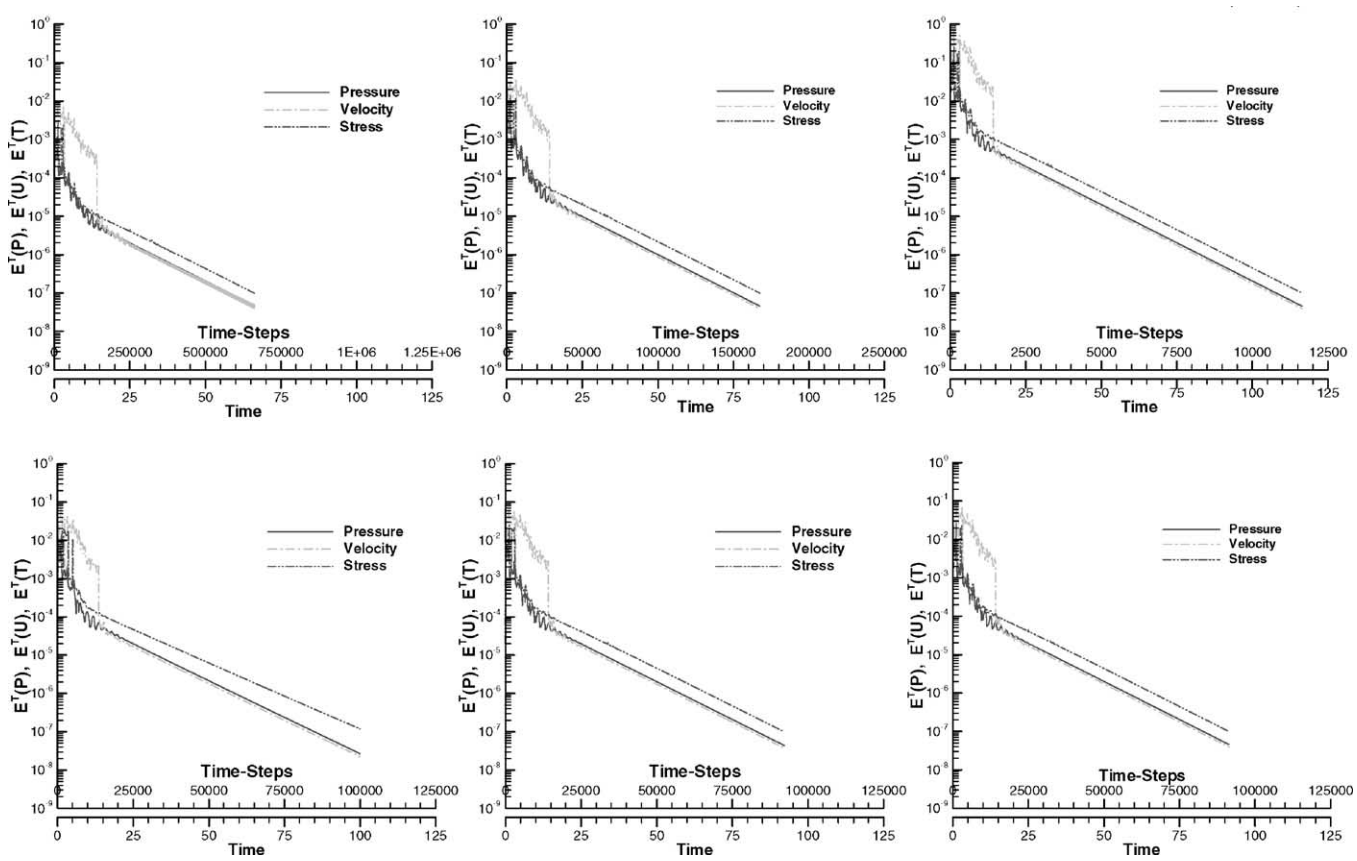

Fig. 3. Compressible flow error norm convergence history for velocity $E^T(U)$, pressure, $E^T(P)$, and stress $E^T(T)$, mesh M1; *We* = 0.1, W&K, quiescent ic. Top: m_{itn} = 5, $\Delta t = 10^{-4}$, 5×10^{-4}, 10^{-2}. Bottom: $\Delta t = 10^{-3}$, m_{itn} = 1, 3, 5.

sults demonstrate that history convergence norm increments are relatively insensitive to adjustment in time-step beyond 10^{-3} and mass iteration number greater than 3. As stability is maintained, it is apparent that by increasing time-step value (interpreted as a fraction of the local Courant number), less time-steps and effort are demanded to achieve a specified relative tolerance level (10^{-7}) equating to steady-state. An important observation concerns the start-up phase. There, some oscillation is apparent in history tolerance, as anticipated for Waters and King kinematic start-up conditions (representative for straight channels). These oscillations are damped away rapidly, whilst the flow evolves to a steady-state, independent of the parameter settings employed.

4.1.2. Incremental continuation in Weissenberg number (incompressible flow)

Next, we turn attention to incompressible viscoelastic computations. A well-recognised and successful strategy to reach a stable steady-state at larger Weissenberg number levels (current target, *We* = 1.0) is to employ *incremental continuation in Weissenberg number* (order zero continuation). This procedure is illustrated through sample results in Fig. 4 with numerical parameters set throughout of (($t = 10^{-3}$, m_{itn} = 3, mesh M2). In this manner, and commencing at the outset from a quiescent state we first gather a solution at *We* = 0.1. Subsequently, the *We* = 0.1 steady-state solution is taken up as the initial starting phase, to derive a solution for *We* = 1.0. For models such as Oldroyd, a limiting level of Weissenberg number (We_{crit}) is commonly encountered in such complex flows (see [2,12,27]). Here, we restrict ourselves to validation at attainable solution levels of unity, to draw out and contrast algorithmic properties of the various alternative implementations. Even at the level of *We* = 1.0, attempting a direct solution procedure (mimicking true time evolution) and starting from a quiescent state, reveals a persistent periodic non-convergence pattern in convergence history, as demonstrated in Fig. 4b. This is a common oscillatory feature at peak *We*-levels with many stable algorithms, where monotonic convergence lies on a stability threshold, dependent upon the size of initial perturbation placed upon the system (given fixed discrete parameters of mesh size and time-step). In like manner, divergence at larger *We*-values would ensue.

4.1.3. Under-relaxation procedure (incompressible flow)

Numerical instability, exposed through temporal convergence history tolerances, may be attributed to spatial or temporal discretization error [11]. Here, stabilization methods, adequate for steady equation systems, may prove ineffective for unsteady systems. Moreover, approximation

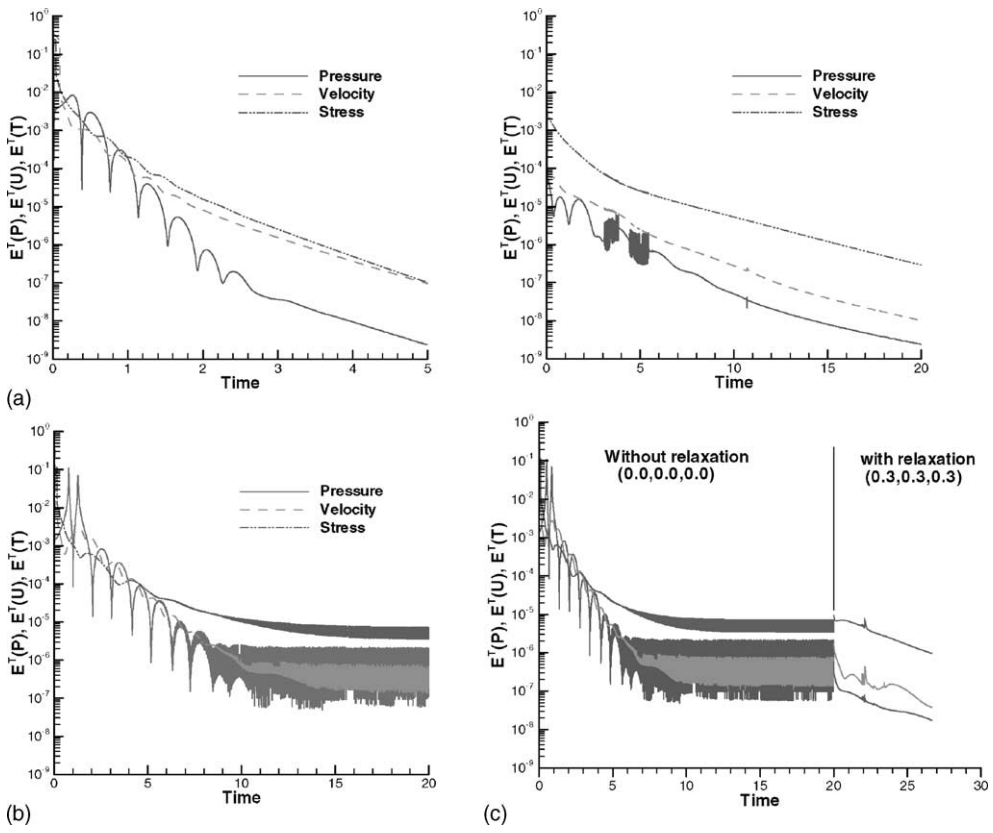

Fig. 4. Incompressible flow error norm convergence history for velocity, $E^T(U)$, pressure, $E^T(P)$, and stress $E^T(T)$, mesh M2; (a): Top left: *We* = 0.1, W&K, quiescent ic. Top right: *We* = 1.0 ic. from *We* = 0.1. Middle (b): *We* = 1.0, from quiescent ic. Bottom (c): output of (b), introducing under-relaxation.

error accumulated through the equation splitting during the fractional-staged procedure, may itself be a source of instability. Fietier et al. [12] have investigated numerical stability and presented time-dependent algorithms for viscoelastic flows, employing spectral element methods. In their study, some stabilization strategies are proposed for flow in simple geometrical configurations. One such proposal is a filtering technique, applied after each time step in an element-by-element fashion on both velocity and stress fields. Still further suggestions for stabilization procedures may be found elsewhere [2,9].

Through the current implementation, numerical stability can be sustained to larger *We*-levels, by appealing to solution under-relaxation. This may adjust the transient representation, to yield the steady-state solution (see pseudo time-stepping, [26]). This is demonstrated starkly in Fig. 4c, where solution under-relaxation is applied equally to all variables $\{r_U, r_(, r_P\}$, at the end of a complete time-step loop. History convergence tolerance oscillations are dramatically removed and monotonic convergence is essentially recovered. We observe that such a relaxation ploy may be interjected on each fractional-stage equation within the time-step loop, so that, solution relaxation may be interpreted via time-step scaling upon each equation-stage time-step (local time-step, per equation). The reader is referred to Appendix for more details. Hence, one arrives at the justification for adjustable internal time-steps [28], to be judged as acting on each fractional-stage solution variable and indeed, expressing dependency upon the mesh selected (fraction of the Courant number).

For viscoelastic incompressible counterparts, we consider the consequences of under-relaxation in some greater detail to gather optimality. To this end, again we adopt mesh M2, and target *We* = 1.0 solutions from quiescent initial conditions. Fig. 5a presents the convergence history scenario without relaxation, for ease of comparison. End-of-3-stages relaxation factors (r_i, per variable i) are applied to the solution field of the form:

$$\chi^{n+1}_{\text{relax}} = r_i \chi^n + (1 - r_i)\chi^{n+1} \tag{29}$$

Convergence histories for constant parameter-setting with $\{r_U, r_\Delta, r_P\} = \{0.3, 0.3, 0.3\}$ are provided in Fig. 5b. This choice is insufficient to damp the persistent oscillatory pattern that has emerged. An optimal level is observed at $\{0.7, 0.7, 0.7\}$ in Fig. 5c, which has the desired suppression and smoothing effect over the prior oscillatory pattern. One may isolate the influence of relaxation to each individual variable (and stage thereby). So, for example, the setting of $\{0.7, 0.7, 0.0\}$ of Fig. 5d reveals insensitivity according to r_P (hence, on (t_P scaling). As demonstrated in Appendix, under-relaxing the local time-step (on velocity) at stage-1 is conveyed to stage-2 local time-step, even without under-

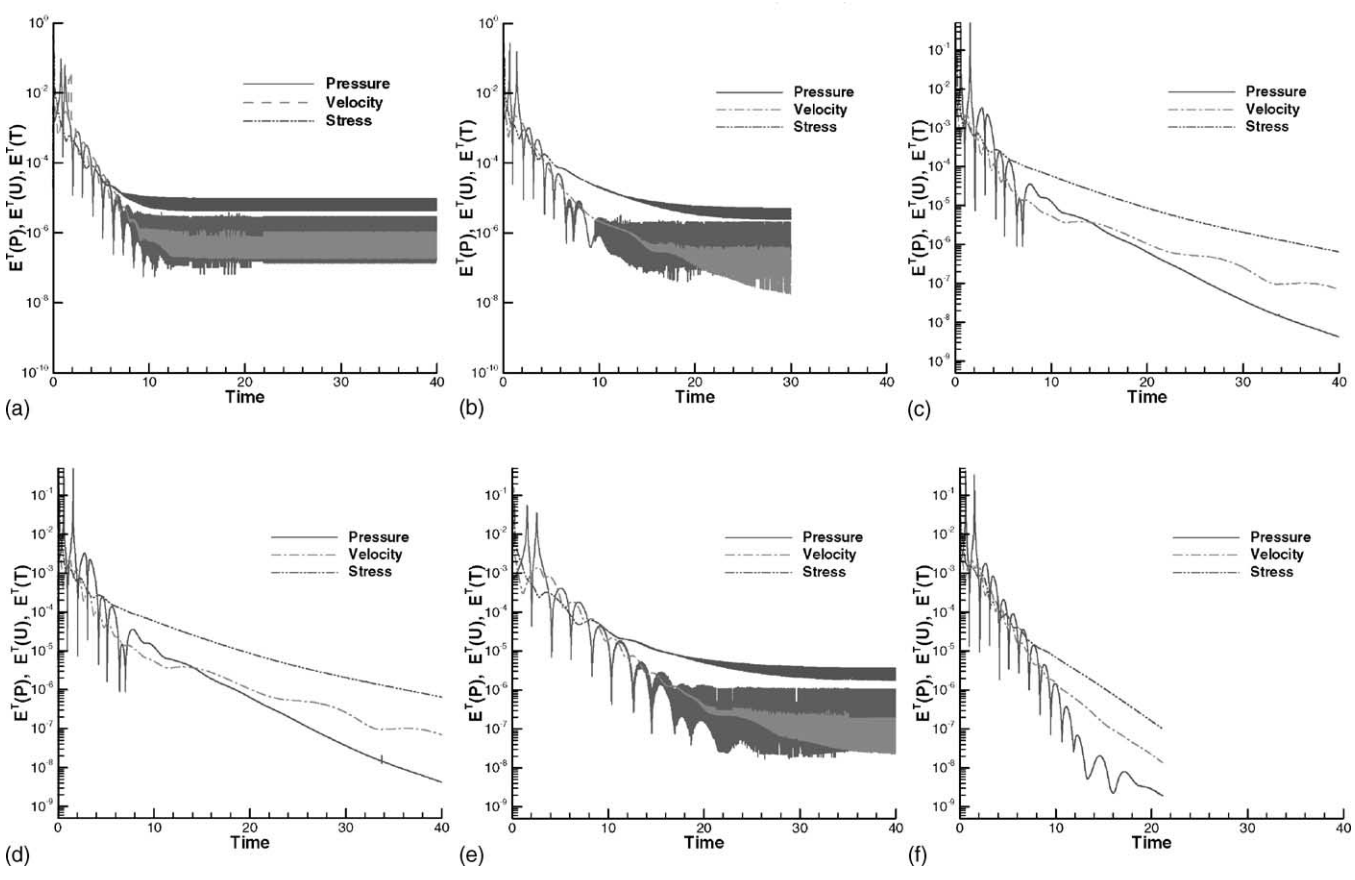

Fig. 5. Incompressible flow error norm convergence history for velocity $E^T(U)$, pressure $E^T(P)$, and stress $E^T(T)$, mesh M2; We = 1.0, W&K, quiescent ic. ($\Delta t = 10^{-3}$, $m_{\text{itn}} = 5$) with relaxation parameters r_U, r_τ, r_P as (a): (0.0, 0.0, 0.0), (b): (0.3, 0.3, 0.3), (c) (0.7, 0.7, 0.7) (d): (0.7, 0.7, 0.0), (e): (0.0, 0.7, 0.0), (f): (0.7, 0.0, 0.0).

relaxing the pressure variable. In contrast, removing velocity under-relaxation, with {0.0, 0.7, 0.0}-choice, demonstrates in Fig. 5e, the crucial role of this factor alone: optimal r_U = 0.7. Removing stress under-relaxation with {0.7, 0.0, 0.0}-setting (as in Fig. 5f) accelerates temporal convergence rates by 50%, achieving the tolerance target in half the time. One concludes, that primarily, only velocity relaxation should be applied. Finally, applying velocity under-relaxation with optimal factors for mesh M2: {0.7, 0.0, 0.0} at end-of-first-stage or at end-of-third-stage (end-of-complete-stage cycle) delivers identical history tolerance behaviour, as demonstrated in Fig. 6. This confirms the crucial impact and importance of

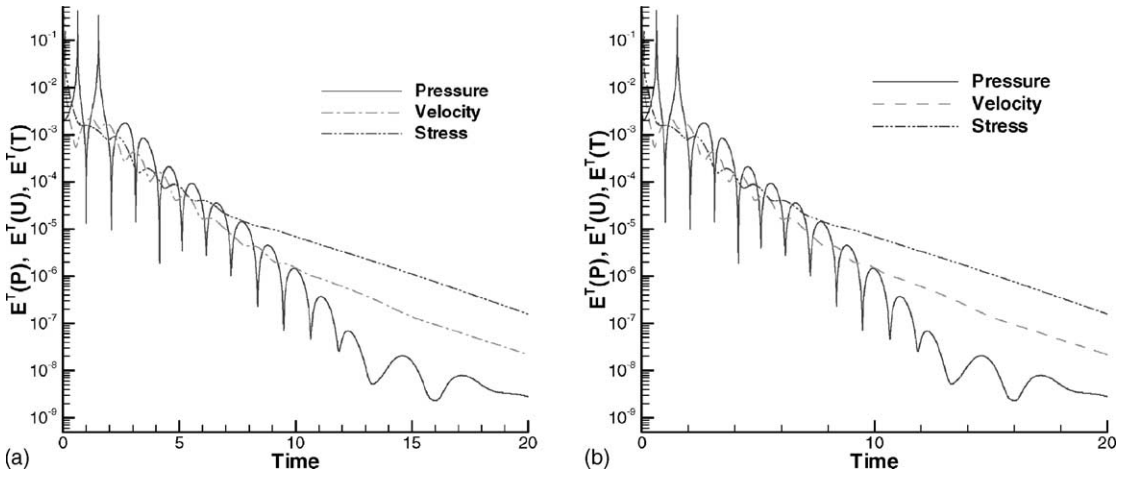

Fig. 6. Incompressible flow error norm convergence history for velocity $E^T(U)$, pressure $E^T(P)$, and stress $E^T(T)$, mesh M2; We = 1.0, W&K, quiescent ic. (for velocity $E^T(U)$, pressure $E^T(P)$, and stress $E^T(T)$, We = 1.0, Re = 1.0. h-Refinement (a, b and c) for weakly-compressible with $(m,B) = (10^4,10^4)$. Different flow scenarios, based on mesh M3 illustrated in d: incompressible, e: weakly-compressible and f: compressible with $(m,B) = (4,10^2)$.

under-relaxation upon stage-1 equations, prior to the remaining fractional-stages within the time-step loop.

4.1.4. Under-relaxation: incompressible, weakly-compressible, and compressible

Based upon the above remarks, we illustrate, in Fig. 7a–c, the different history tolerance results across the series of three meshes employed for weakly-compressible ($(m,B) = (10^4,10^4)$). The history convergence tolerances across meshes for incompressible flows are similar in form to those of weakly-compressible and are omitted. Mesh (h) refinement has no noticeable effect on history tolerances for compressible ($(m,B) = (4,10^2)$) flows, following the form shown for mesh M3 in Fig. 7f. Results are also illustrated across flow scenarios in Fig. 7d–f (incompressible, weakly-compressible and compressible flows). For all cases a $We = 1.0$ is targeted from a quiescent initial state. The first observation is that, independent of mesh employed or flow type, convergence history tolerance always commences with an oscillatory pattern, typical of transient start-up conditions. About 10–15 time units are necessary to dampen these oscillations and recover a smooth convergence pattern. For weakly-compressible (as well as incompressible) flows, based on mesh M2 and M3, under-relaxation is necessary to reach the specified tolerance level. As anticipated by reducing mesh size from M2 to M3, optimum levels of the relaxation factors imply lesser need for relaxation. Note that for these flows, a time–step of 10^{-3} is applied, leading to steady-state solutions within 30–50 time units. Here, we point out that the choice of time-step is not only governed by the Courant number restriction, but also by the size of Weissenberg number. For *compressible flow* conditions, relaxation is unnecessary at this level of Weissenberg number, to reach the specific tolerance and enhanced smoothness in convergence is apparent beyond that of the incompressible case, upon the three test meshes (not shown here). This is due mainly to improved equation conditioning at stage-2, through the modifications to accommodate for compressibility considerations (see Eq. (19), M_c and L^ρ). Here, a larger time-step is permitted ($\Delta t = 10^{-2}$). Independent of the spatial discretization employed, a tight window of temporal convergence is observed, displaying a uniform and smooth trend. For compressible flow, independent of meshing, less computational time is demanded to reach a steady-state solution when compared to counterpart incompressible flow settings (30% more rapid). Finally, mesh refinement does not necessarily demand stringent reduction in time-step to reach the desired tolerance level (as is the case in the incompressible/weakly-

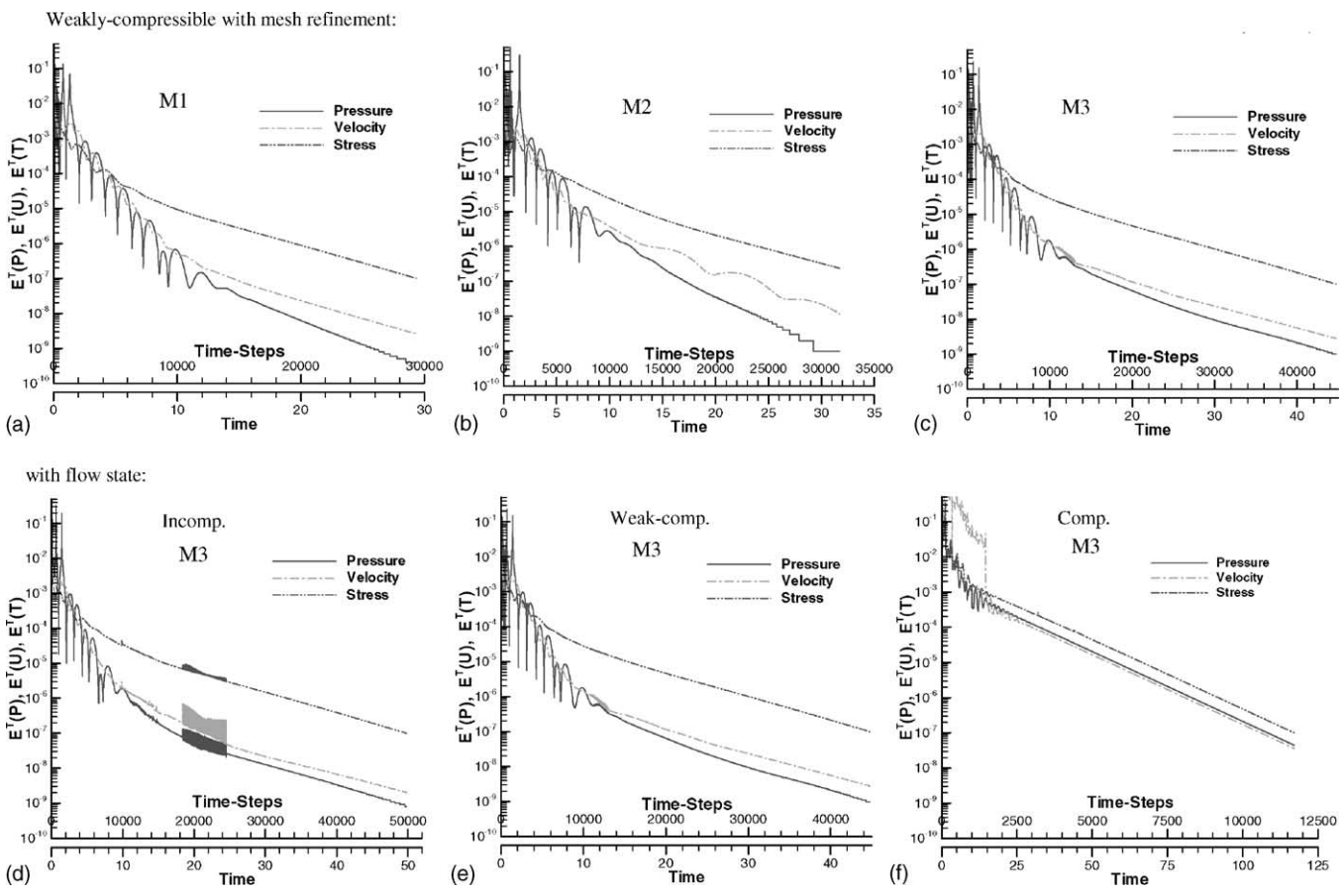

Fig. 7. Error norm convergence history for velocity, $E^T(U)$, pressure, $E^T(P)$, and stress $E^T(T)$, $We = 1.0$, $Re = 1.0$. h-refinement (a–c) for weakly-compressible with $(m,B)=(10^4,10^4)$. Different flow scenarios, based on mesh M3 illustrated in d: incompressible, e: weakly-compressible and f: compressible with $(m,B)=(4,10^2)$.

compressible context). This bodes well for numerical continuation between the different levels of compressibility.

4.2. Mesh (h) refinement

Convergence of solutions in all component variables has been confirmed through mesh refinement on the series of meshes employed. Finally, consistency of the scheme is highlighted by the ability of the scheme to accommodate weakly-compressible flow scenarios. There similar results are derived for incompressible and weakly-compressible representations.

Having established satisfactory convergence trends, independent of flow type or mesh employed, we turn to interrogate field solution quality through pressure, principal stress N_1 (first normal stress-difference) and shear stress contour plots. All our results thus far have been for *We* = 1.0 and *Re* = 1.0. Each variable figure represents nine contour plots. Incompressible flow results are d isplayed on the left, weakly-compressible in the middle and compressible to the right. Solutions based on mesh M1 are illustrated at figure-top, M2 at centre, and M3 over figure-bottom. In this manner and for each variable, it is practical to contrast scheme accuracy, based on mesh refinement, and scheme consistency whilst increasing Mach number (from the incompressible toward the compressible flow regime). In Fig. 8, around the contraction zone, similar pressure contour patterns at equitable levels are observed for incompressible and weakly-compressible representations. Pressure-drop increases with mesh-density in all instances, being slightly higher for weakly-compressible as compared to incompressible flow setting. For the more compressible regime, it is apparent that pressure-drop is higher (about 10%) than with other flow settings, relating directly to compressibility effects. Similar conclusions may be drawn on principal stress contour plots presented in Fig. 9. Here, the maximum level of stress is considerably larger upon mesh M3, when compared with M2 or M1, independent of flow representation. This increase is about 90–95%, indicating the strong presence of a singularity located at the re-entrant corner. Field distributions show little disparity between flow settings upon the remainder of the domain, away from the downstream-wall, increasing thereupon. In shear stress, there is a doubling in maximum stress level between mesh M1 and M3 solutions (typical values *O*(18 units) on M3 compare to *O*(9 units) on M1), indicating again the significant presence of a singularity. Note, that for each variable, the contour plots display similar patterns through mesh refinement or flow-type under consideration. Incompressible stress fields are corroborated by their close agreement with those in the published literature (see [12,13]).

Based on the finest mesh M3, streamlines contours plots for incompressible and compressible flows are displayed in Fig. 10. Similar incompressible streamlines contours at *We* = 1.0 are presented in reference [13]. Contour distributions show little disparity between flow settings, except at the centre of the vortex zone, where the stream function peaks ($*10^{-4}$) increase from −1.86 (compressible) to −2.06 (incompressible), and stream function maxima increase from 1.00 (incompressible) to 1.28 (compressible). Finally, for compressible flow based on mesh M3, density and Mach

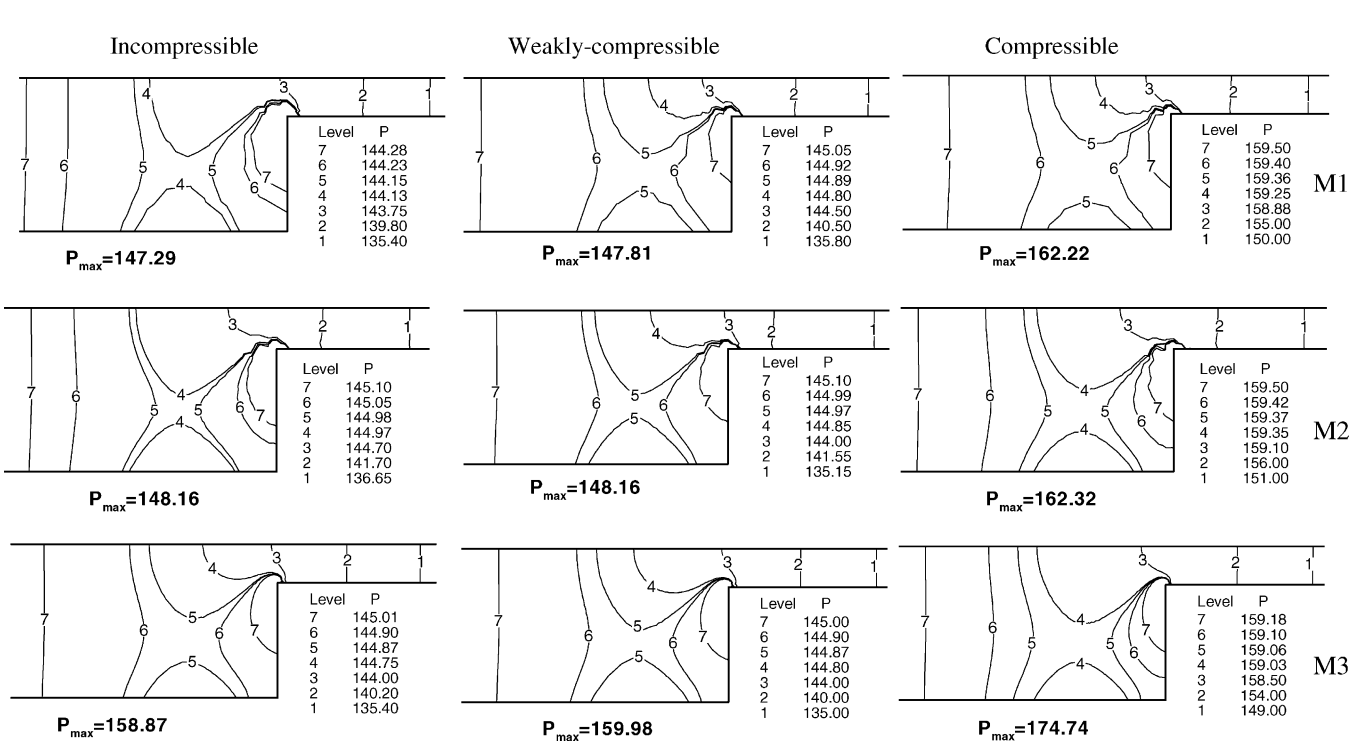

Fig. 8. Pressure *P* contours, *h*-refinement (M1: top, M2: centre, M3: bottom), left: incompressible, middle: weakly-compressible and right: compressible flow. *We* = 1.0, *Re* = 1.0.

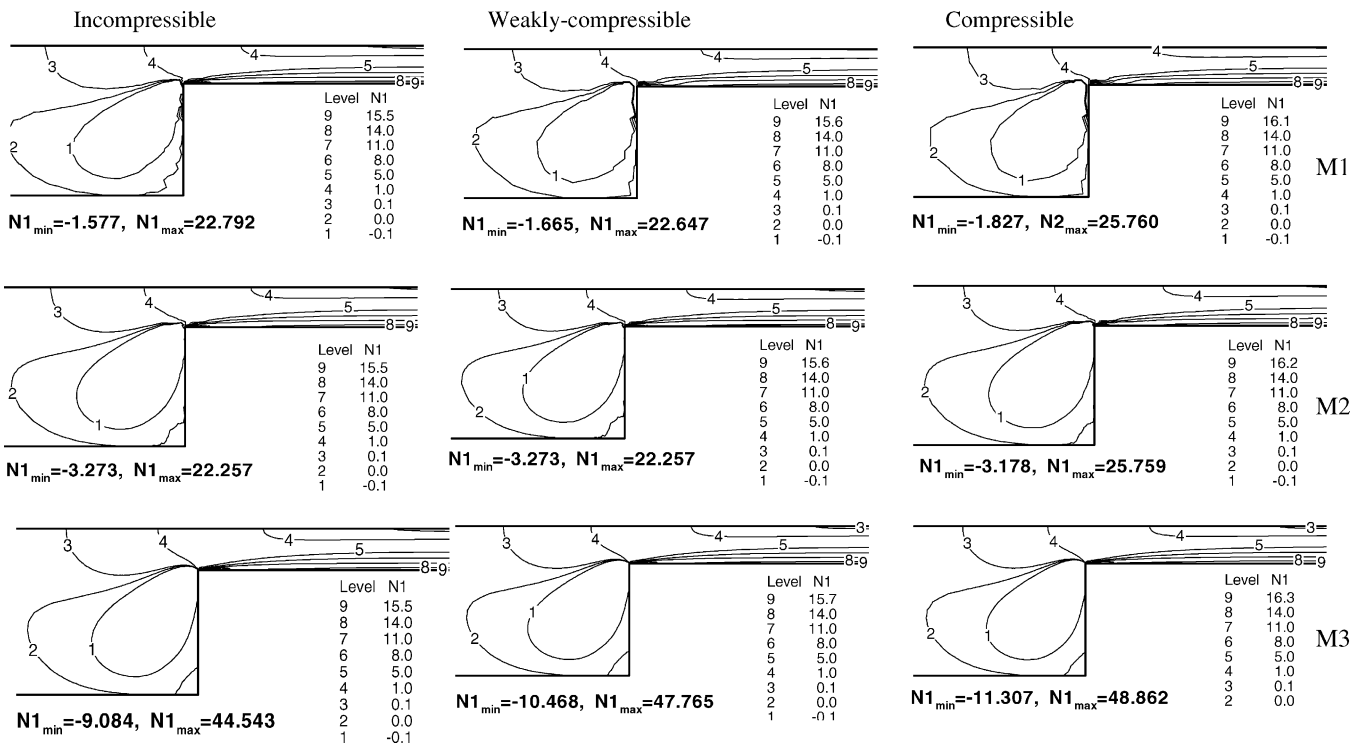

Fig. 9. Principal stress N_1 contours, *h*-refinement (M1: top, M2: centre, M3: bottom), left: incompressible, middle: weakly-compressible and right: compressible flow. *We* = 1.0, *Re* = 1.0.

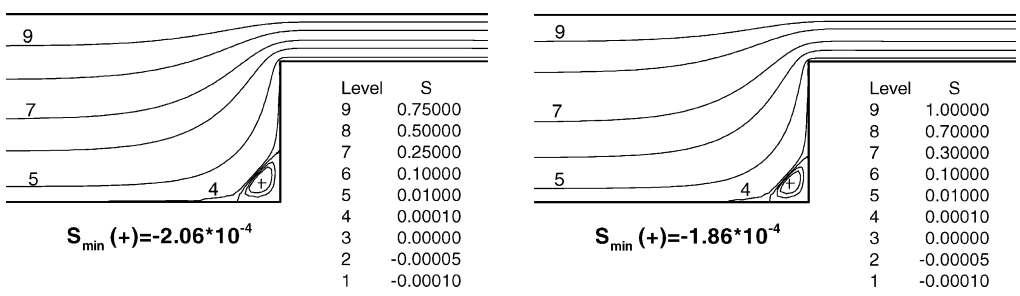

Fig. 10. Streamline contours, incompressible (left) and compressible flow (right), mesh M3. *We* = 1.0, *Re* = 1.0.

number contours are provided in Fig. 11. Note, density contours are non-parallel in the upstream or downstream channel sections (as with pressure). This is due to the fact that under viscoelastic consideration, density is a function of the augmented pressure, which takes into account the trace of stress (see Tait equation Eq. (5)). An increase of 28% in density arises between the inlet and outlet. Outlet Mach numbers of *Ma* = 0.093 are approached under such compressible flow conditions.

4.3. Stress development

To highlight the re-entrant corner solution for *We* = 1.0 solutions, stress profiles (τ_{xx}, τ_{xy}, τ_{yy}) at y = 0.3 units (see

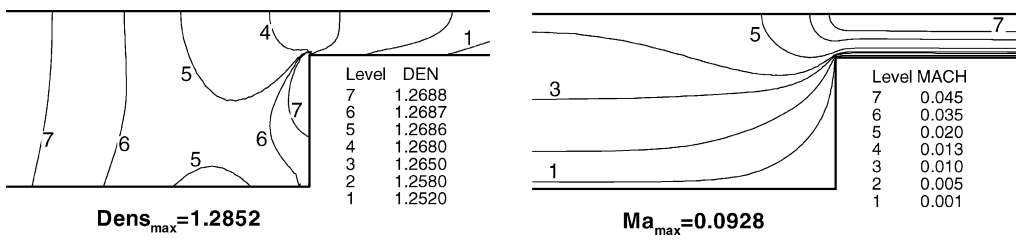

Fig. 11. Density (left) and Mach number (right) contours for compressible flow setting, mesh M3. *We* = 1.0, *Re* = 1.0.

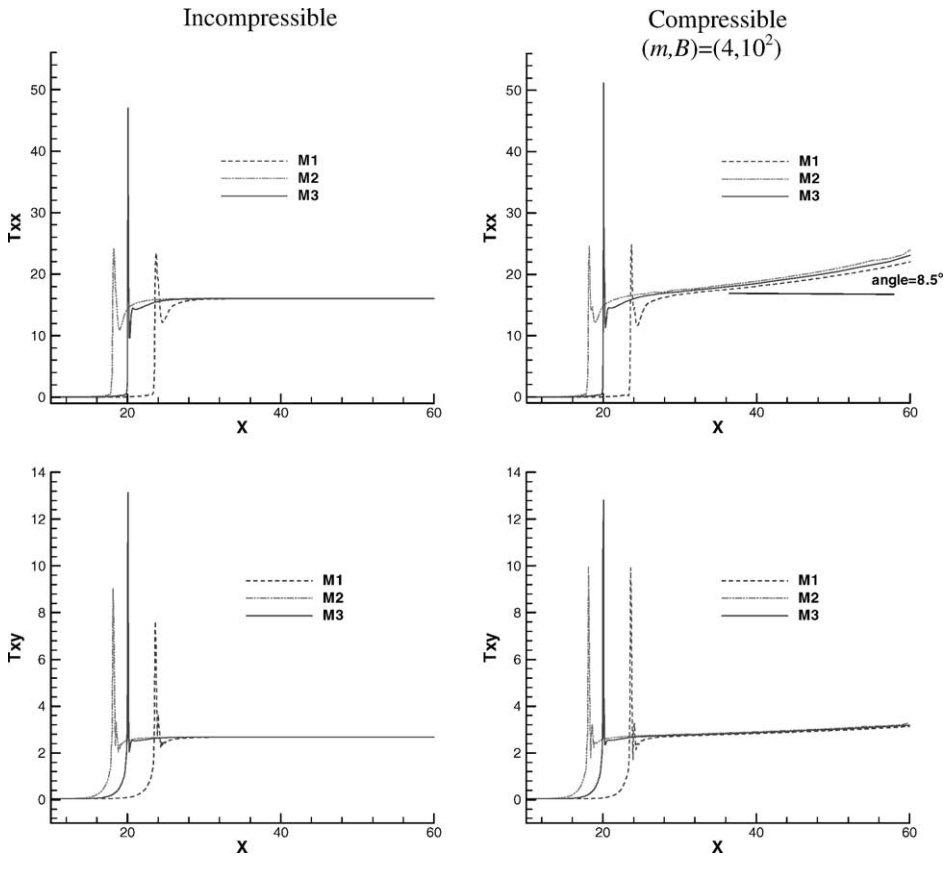

Fig. 12. Stress profiles (τ_{xx}: top, τ_{xy}: bottom) along $y = 0.3$, different meshes (M1, M2, M3) and flow scenarios (incompressible: left, compressible: right). *We* = 1.0, *Re* = 1.0.

Fig. 1) are illustrated in Fig. 12, across the three meshes and flow scenarios. For clarity in plotting, a shift in the position of the re-entrant corner for the different meshes has been applied. As anticipated there are no noticeable differences in stress plot results for incompressible and weakly-compressible representations, and also across all regimes for τ_{yy}; hence these are discarded accordingly. All plots reflect a prominent stress peak at the re-entry corner. The level of this peak increases with mesh refinement, and also, with greater levels of compressibility.

For the more compressible flow, a major feature lies in the growth of stress, τ_{xx}, near the boundary along the downstream wall (monotonic growth at an angle 8.5°). A corresponding feature arises to a lesser degree in the shear stress component, τ_{xy}. Such an expansion/growth of boundary stress is non-existent in incompressible or weakly-compressible flow settings. Finally, note that compressibility does not mitigate the strength of the corner solution singularity in stress.

Careful analysis of the boundary stress and stress profile development is conducted upon the principal first normal stress-difference, N_1. To this end, variation in stress across the channel, cross-section $y = 3$ to $y = 4$ units, is plotted at different downstream positions (see Fig. 13). Results are presented in Fig. 13b–c based on mesh M3 for the incompressible and compressible flow representations. For the incompressible flows, beyond a downstream position of $x = 30$ units there is barely any discernible variation in the stress field through the channel cross-section. In contrast, there is more widening and gradual growth of stress-profiles along the wall for the more compressible flow conditions. In Fig. 14, where for plotting clarity the cross-section dimension has been zoomed some forty times, three-stress levels (contour values, 1, 5 and 15 units for τ_{xx}, and 0.5, 1.8 and 2.6 units for τ_{xy}) are plotted along the downstream channel wall. We observe the rapid onset of the boundary layer structure just beyond the contraction zone (contraction at $x = 22$ units) for all flows. The sustained growth of stress along the downstream direction is detected off the channel wall into the flow.

As an overall remark, the main disparity between incompressible and compressible flow representations is related to the levels of stress peak at the re-entry corner and the monotonic stress growth along downstream wall and flow direction. In the incompressible state, such growth manifests a constant (limiting) level and width, established fairly rapidly beyond the corner after the stress boundary layer has formed.

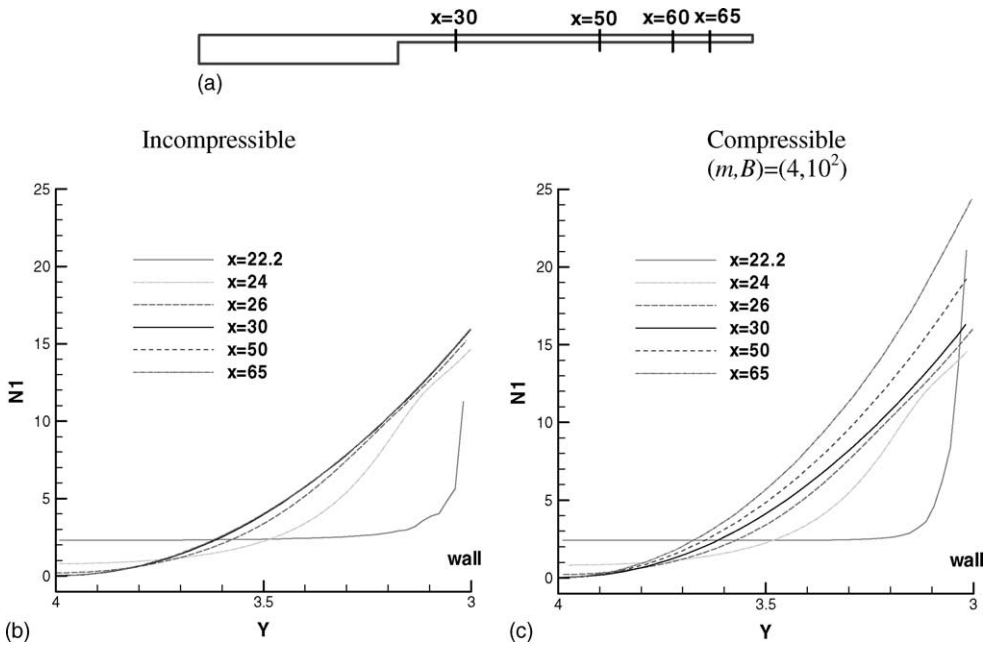

Fig. 13. (a) Profile sampling x-positions for principal stress N_1 along downstream channel. (b–c) Principal stress N_1-profiles across downstream channel section, sampling x-positions, mesh M3, b: incompressible, c: compressible. We = 1.0, Re = 1.0.

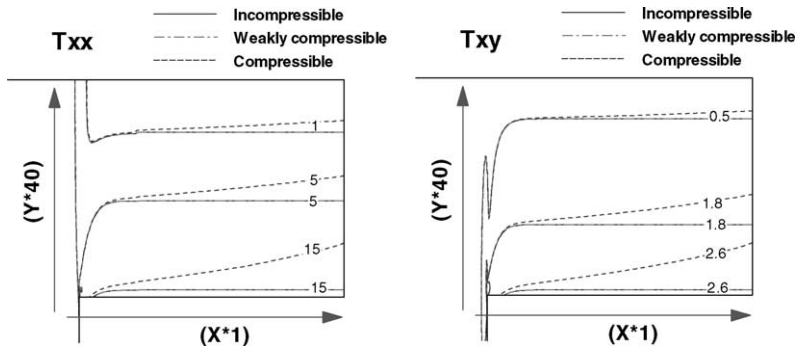

Fig. 14. Stress profiles: τ_{xx} (right) and τ_{xy} (left) along downstream channel. Boundary layer growth for incompressible, weakly-compressible and compressible flow conditions, mesh M3. We = 1.0, Re = 1.0 (scaling indicated).

5. Conclusions

This study has provided new insight into the finite element modelling of viscoelastic compressible flows, where we have consciously focused on the Oldroyd model, the Tait equation of state, and planar contraction flows. We have proposed a fresh look at pressure-correction type formulations to tackle such a setting, so utilising pressure as a primary variable emanating from conventional incompressible flow representation. In this manner, we have accurately and consistently resolved both evolutionary and steady-state flows, covering the low Mach number regime. A unified (single) finite element scheme is advocated, with flexibility to cover compressible, weakly-compressible, and incompressible flow situations. Various aspects of study have revealed: (i) the role and importance of relaxation across fractional-staged equations; (ii) sensitivity of the scheme to selection of $\{\Delta t, h, m_{\text{itn}}\}$-parameters, within the different flow settings; (iii) convergence trends and contrast of flow field response.

A major observation is the heavy-side influence that compressible equation structure has on temporal, monotonic, in-phase convergence properties. This extends equally to the asymptotic limit and weakly-compressible scenario, that mimics (slightly) incompressible flow ($Ma \approx 10^{-4}$). Hence, the weakly-compressible assumption may be usefully employed to numerically improve convergence properties for incompressible viscoelastic solutions.

Pressure drops rise when greater levels of compressibility are incorporated (here by order 10%). We observe the fact that solution singularity (stress at re-entrant corner) may actually increase in a more compressible setting, whilst downstream-wall stress profiles broaden along the wall, away from initial inception of the boundary layer, just beyond the re-entrant corner. This is in stark contrast to the incompressible sce-

nario, where wall-stress profiles sustains their initial width far downstream. Stress boundary layers are provoked almost directly beyond the re-entrant corner in all flows studied. Extensions to the current study shall be oriented towards seeking solutions upto critical levels of Weissenberg number, and considering temporal adjustment of the compressible parameter set.

Acknowledgements

The financial support of EPSRC grant GR/R46885/01 is gratefully acknowledged.

Appendix A

Appendix: Fractional staged equations and relaxation procedure

The relaxation procedure may be applied at different TGPC stages and has a direct effect on the local time-step-stage value. To clarify this point, let us consider the first and second stages of TGPC scheme for *incompressible* fluid in compact matrix form:

$$A_U(U^* - U^n) = \Delta t b_U, \tag{A.1}$$

$$K(P^{n+1} - P^n) = \frac{1}{\theta\Delta t} L U^*. \tag{A.2}$$

Here, n denotes the time level, (t the local time-step, U*, U, P, nodal vectors of non-divergence-free velocity, velocity and pressure, respectively, b_U the right-hand-side of stage-1b. A_U and K are velocity and pressure governing matrices (mass and stiffness).

In order to relax velocity by at the end of stage-1, we introduce a relaxed non-divergence-free velocity, viz.:

$$\tilde{U}^* = \alpha_u U^* + (1 - \alpha_u)U^n = U^n + \alpha_u(U^* - U^n). \tag{A.3}$$

Note, for convenience of representation we may interpret the relaxation parameter of the text via taking advantage of stage-1b equation (Eq. (A.1)), and re-arranging Eq. (A.3), yields:

$$A_U(\tilde{U}^* - U^n) = \alpha_u \Delta t b_U \tag{A.4}$$

An under-relaxed representation for equation stage-1b, casting velocity solution relaxation onto the local time-step, via scaling with factor.

To enforce relaxation upon stage-2 alone, we introduce a relaxed pressure solution-component:

$$\tilde{P}^{n+1} = \alpha_P P^{n+1} + (1 - \alpha_P)P^n = P^n + \alpha_P(P^{n+1} - P^n). \tag{A.5}$$

Revisiting stage-2 equation (Eq. (A.2)) with relaxation, and taking into account Eq (A.5), we may gather a relaxed stage-2 equation:

$$K(\tilde{P}^{n+1} - P^n) = \frac{\alpha_P}{\theta\Delta t} L U^*. \tag{A.6}$$

Thus, at this fractional-equation stage, relaxing stage 2 is equivalent to scaling the local pressure equation time-step by.

Finally, one may appreciate that relaxing velocity alone (and not pressure), conveys some relaxation into the local time-step at stage-2, through in the rhs-vector. Reconsidering the relaxed non-divergence-free velocity ($\tilde{U}^*$) of Eq. (A.3) and applying the discrete matrix equivalent to the divergence operator, yields:

$$L\tilde{U}^* = (1 - \alpha_u)LU^n + \alpha_u LU^*, \tag{A.7}$$

which will impact upon the system through the stage-2 equation accordingly,

$$K(P^{n+1} - P^n) = \frac{1}{\theta\Delta t} L\tilde{U}^* = \frac{\alpha_U}{\theta\Delta t} LU^* + \frac{(1 - \alpha_U)}{\theta\Delta t} LU^n, \tag{A.8}$$

Here, we may appeal to the continuity equation to neglect the term $LU^n \approx 0$ on the right-hand-side of Eq. (A.8), giving:

$$K(P^{n+1} - P^n) \approx \frac{\alpha_U}{\theta\Delta t} LU^*. \tag{A.9}$$

Therefore, we appreciate that by relaxing velocity at stage-1, we impart scaling on local time-steps at both stage-1 and stage-2. Similar arguments hold for the compressible flow context.

References

[1] J. Keshtiban, F. Belblidia, M.F. Webster, Second-order schemes for steady weakly-compressible liquid flows, Computer Science Technical Report, CSR4-2003.
[2] F.P.T. Baaijens, Mixed finite element methods for viscoelastic flow analysis: a review, J. Non-Newtonian Fluid Mech. 79 (1998) 361–385.
[3] M.J. Crochet, A.R. Davis, K. Walters, Numerical Simulation of Non-Newtonian Flow, Elsevier, Amsterdam, 1984.
[4] R. Keunings, Simulation of viscoelastic flow, in: C.L. Tucker (Ed.), Computer Modeling for Polymer Processing, Hanser, Munich, 1989, pp. 404–469.
[5] K. Walters, M.F. Webster, The distinctive CFD challenges of computational rheology, Int. J. Num. Meth. Fluids, special issue (Keynote: ECCOMAS), Swansea, 1–26, 2001.
[6] T.N. Phillips, A.J. Williams, Viscoelastic flow through a planar contraction using a semi-Lagrangian finite volume method, J. Non-Newtonian Fluid Mech. 87 (1999) 214–246.
[7] P.J. Oliveira, F.T. Pinho, G.A. Pinto, Numerical simulation of non-linear elastic flows with a general collocated finite volume method, J. Non-Newtonian Fluid Mech. 79 (1998) 1–43.
[8] A. Baloch, P. Townsend, M.F. Webster, On the simulation of highly elastic complex flows, J. Non-Newtonian Fluid Mech. 59 (2–3) (1995) 111–128.
[9] H. Matallah, P. Townsend, M.F. Webster, Recovery and stress-splitting schemes for viscoelastic flows, J. Non-Newtonian Fluid Mech. 75 (1998) 139–166.
[10] J.M. Marchal, M.J. Crochet, Hermitian finite elements for calculating viscoelastic flow, J. Non-Newtonian Fluid Mech. 20 (1986) 187–207.
[11] R. Guènette, M. Fortin, A new mixed finite element method for computing viscoelastic flows, J. Non-Newtonian Fluid Mech. 60 (1995) 27–52.

[12] N. Fietier, M.O. Deville, Time-dependent algorithms for the simulation of viscoelastic flows with spectral element methods: applications and stability, J. Comp. Phys. 186 (2003) 93–121.
[13] P. Wapperom, M.F. Webster, A second-order hybrid finite-element/volume method for viscoelastic flows, J. Non-Newtonian Fluid Mech. 79 (1998) 405–431.
[14] M. Aboubacar, M.F. Webster, A cell-vertex finite volume/element method on triangles for abrupt contraction viscoelastic flows, J. Non-Newtonian Fluid Mech. 98 (2001) 83–106.
[15] G.C. Georgiou, The time-dependent compressible Poiseuille and extrudate-swell flows of a Carreau fluid with slip at the wall, J. Non-Newtonian Fluid Mech. 109 (2003) 93–114.
[16] E.A. Brujan, A first-order model for bubble dynamics in a compressible viscoelastic liquid, J. Non-Newtonian Fluid Mech. 84 (1999) 83–103.
[17] M. Ranganthan, M.R. Mackley, P.H.J. Spitteler, The application of the multipass rheometer to time-dependent capillary flow measurements of a polyethylene melt, J. Rheol. 43 (1999) 443–451.
[18] K.E. Barrett, A.C. Gotts, Finite element analysis of a compressible dynamic viscoelastic sphere using FFT, Comput. Struct. 80 (2202) 1615–1625.
[19] P.G. Tait, HMSO, London 2(4), 1888.
[20] C. Hirsch, Numerical Computation of Internal and External Flows, Computational methods for inviscid and viscous flows, Wiley, 1999.
[21] B. Poling, J. Prausnitz, J. O'Connell, Properties of Gases and Liquids, 5th edn., McGraw-Hill, 2000.
[22] D. Ding, P. Townsend, M.F. Webster, The iterative solution of Taylor-Galerkin augmented mass matrix equations, Int. J. Num. Meth. Eng. 35 (1992) 241–253.
[23] D.M. Hawken, H.R. Tamaddon-Jahromi, P. Townsend, M.F. Webster, A Taylor-Galerkin based algorithm for viscous incompressible flow, Int. J. Num. Meth. Fluids 10 (1990) 327–351.
[24] T.N. Phillips, A.J. Williams, Comparison of creeping and inertial flow of an Oldroyd-B fluid through planar and axisymmetric contractions, J. Non-Newtonian Fluid Mech. 108 (2002) 25–47.
[25] N.D. Waters, M.J. King, Unsteady flow of an elastico-viscous liquid, Rheol. Acta 9 (1970) 245–355.
[26] E.O. Carew, P. Townsend, M.F. Webster, Taylor-, Galerkin algorithms for viscoelastic flows: application to a model problem, Num. Meth. Partial Diff. Eqns. 19 (1994) 171–190.
[27] A.M. Alves, P.J. Oliveira, F.T. Pinho, Benchmark solutions for the flow of Oldroyd-B and PTT fluids in planar contractions, J. Non-Newtonian Fluid Mech. 110 (2003) 45–75.
[28] P. Nithiarasu, O.C. Zienkiewicz, On stabilization of the CBS algorithm: internal and external time steps, Int. J. Num. Meth. Eng. 48 (2000) 875–880.